A DFT study of atomic structure and adhesion at the Fe(BCC)/Fe$_3$O$_4$ interfaces

M.D. Forti [a,b], P.R. Alonso [a,b], P.H. Gargano [a,b], P.B. Balbuena [c], G.H. Rubiolo [a,b,d,*]

[a] Gerencia Materiales, Comisión Nacional de Energía Atómica, Avenida General Paz 1499, San Martín B1650KNA, Buenos Aires, Argentina
[b] Instituto Sabato–UNSAM/CNEA, Av. G. Paz 1499, San Martín B1650KNA, Buenos Aires, Argentina
[c] Department of Chemical Engineering, Texas A&M University, College Station, TX 77843, USA
[d] Consejo Nacional de Investigaciones Científicas y Tecnológicas, CONICET, Argentina

A B S T R A C T

The adhesion at Fe/Fe3O4 interface is one of the critical pieces of information that is often lacking upon designing the protective magnetite layer on the inner surfaces of carbon steel piping or upon modeling the scale removal mechanism for optimization of industrial descaling of the wire or strip surface of carbon steel after hot rolling process. In this context, we have performed ab initio DFT calculations to determine the atomic structure, work of separation (γ), and bonding character of the Fe(001)/Fe$_3$O$_4$(001) interface. Three candidate interface geometries were considered, including Fe and FeO$_2$ terminations of the oxide. The minimization of the forces resulted in substantial changes to the atomic structure of the metal and oxide layer at both side of the interface, and also of the subsurface layer of the oxide in the case of Fe-terminated oxide slab. Moreover, the relaxation of the geometry in one of the two considered Fe-terminated oxide interface leads to completely unstable interface structures. By applying several methods of analysis, we have thoroughly characterized the electronic structure and have determined that the dominant bonding mechanism is the metallic-ionic interaction between the iron atoms of both metal and oxide slabs. Our calculations predict $\gamma \approx 1.42$ J/m^2 regardless of the interfacial stoichiometry.

© 2015 Elsevier B.V. All rights reserved.

1. Introduction

Unstable metals dissolve by active corrosion in an oxidizing environment (air, water). They become "passive" if they substantially resist corrosion under conditions where the bare metal would react significantly. This behavior is due to the inhibition of active dissolution by a more or less spontaneous formation of a dense passive film of limited ionic conductivity. Passive films are formed from the metal itself and components of the environment, usually currentless in water and in contact with air or anodically with water. The anodic current density may be supplied from an outer circuit or is compensated by cathodic currents like hydrogen evolution or oxygen reduction at open circuit conditions. In general, the term "passive film" is used in connection with films formed in aqueous solution, but in electronics and other fields, the definition includes all protective films against corrosion, even if they are deposited by any other technique rather than anodization, e.g., physical vapor deposition, or oxidation by oxygen or steam [1].

In many aqueous environments, the passive film is in constant exchange of species with the electrolyte and consequently alters in thickness and composition. Among the factors that influence the passive film, it is worth to mention the anodic potential, the presence of halides in the electrolyte, the pH, and the temperature [2]. In most cases, at room temperature, the passive film grows with increasing anodic potential at the rate of 1–3 nm/V. In particular, the passive film on iron in aqueous solutions grows up to about 5 nm at potentials prior to the onset of oxygen evolution [3]. A mildly alkaline borate buffer became the most common solution used to study the growth of the passive film on iron surfaces; the structure of the film shows an inhomogeneous composition along its thickness [4]. From the survey of the literature, it is apparent that the most frequently quoted candidate structure for the passive film on iron is closely related to the spinel structures of magnetite (Fe$_3$O$_4$) [5–7]. The passive films formed on iron at elevated temperatures differ markedly from those formed at room temperature. Oxide layers with a thickness of 100–200 nm have been reported to form at T > 150 °C. This increase in thickness with increasing temperature can be connected with the formation of a duplex film. The duplex film consists of a compact inner layer of iron spinel and a more porous outer layer enriched with iron [8].

At ambient air, multi-phase oxide scales evolve on iron surface which are composed of two (below 570 °C) or three (above 570 °C) oxide sub-layers having distinct mechanical properties and growing by different mechanisms. The sub-layer next to the metal is magnetite in the low temperature range while it is wüstite (FeO) for the high

* Corresponding author at: Gerencia Materiales, Comisión Nacional de Energía Atómica, Avenida General Paz 1499, San Martín B1650KNA, Buenos Aires, Argentina.
E-mail address: rubiolo@cnea.gov.ar (G.H. Rubiolo).

temperature range. The oxidation kinetics of iron in air or oxygen is characterized by a rapid initial oxidation and a slower steady long-term oxidation usually following the parabolic rate law [9]. The parabolic rate constants reported for the annealed specimens between 250 °C and 550 °C show an Arrhenius behavior with a transition from one-stage to two-stage oxidation process around 370 °C. For the temperatures higher than 370 °C where the one-stage oxidation process occurs, the maximum thickness of the oxide scale after 12 h is about 400 nm and the thickness ratio between the hematite and magnetite layers is in the range 1:10 to 1:20 [10].

The integrity of the oxide scales formed on carbon steels used for pipelines in industrial plants is of key importance when assessing corrosion resistance of the alloy. The breakdown of the protective passive film, arising from various factors, such as the formation of voids on protective scales, may initiate localized corrosion mechanisms [11]. In addition, particles originated in oxide spallation on pipes surface may cause the erosion or blockage of a remote component of the system. For example, the oxide particles detached from the recirculation pipelines in the primary heat transport system of pressurized heavy water reactors may move with the water and build up radioactive activity elsewhere in the system [12,13].

The oxide scale formed on the wire or strip surface of carbon steel after hot rolling process needs to be removed for subsequent cold rolling, galvanizing, or coating. This oxide scale is generated while the hot coiled wire or strip cools down from about 570 °C until the ambient temperature. The thickness of the oxide scale is in the range of 8–11 μm, and the removal is typically conducted by acid pickling [14]. The contemporary trend is the discouragement of the use of strong acids due to the processing needed to protect the environment. Therefore, it is important to explore mechanical descaling as an alternative method [15]. Mechanical known methods for descaling wire or strip consist in bending on well-adapted rollers [16] or in dry or wet shot blasting [17]. Thus, the descalability of the steel surface is intrinsically linked to the mechanical integrity of the oxide scale [18].

The study of the mechanical integrity of oxide scales has become a major concern during the last few decades ([19] and references therein). A classification of fracture modes has been reviewed by Schütze [19,20] depending on the stresses affecting the oxide scale and crack orientation in relation to metal/oxide interface. The authors reviewed failure criteria for each case. Spallation failure is cited as an example. This failure mode can be found in systems with a weak interface in relation to the oxide, and under compressive stress. Critical conditions for crack nucleation and growth may be modeled [19,20], and it can be seen that interfacial fracture energy must be determined precisely for these models to attain predictive power.

In this context, the adhesion at Fe/Fe$_3$O$_4$ interface is one of the critical pieces of information that is often lacking when designing the protective magnetite layer on the inner surfaces of carbon steel piping in order to minimize further corrosion [13] or when modeling the scale removal mechanism for optimization of industrial descaling conditions [18]. Due to the importance of scale adhesion in these technological issues, several experimental methods were developed to quantify this property but accurate results are scarce and difficult to achieve. Some of them can be mentioned here: the torsion-balance device which is used to measure adhesion forces [21], the inverse blistering test which is used to determine the adhesion of metallic films on oxide substrates [22], the micro-tensile test which is performed inside a scanning electron microscope [23], generally used to measure adhesion of oxide thin films on metallic substrates, and the macro-tensile stress test aided by optical microscopy used to measure adhesion of thick oxide films on metallic substrates [24]. Measurements during the mentioned micro and macro-tensile test consist in recording the fraction of scale which has spalled as a function of strain; afterwards, a mathematical model is used to relate released spalled fraction of surface area with interfacial fracture energy [23–25]. This kind of test was used to determine the only available value, as far as we know, for the

mechanical adhesion energy (work of separation) at the interface between low carbon steel and magnetite [24]. The authors report a value of 2 J/m^2.

Computational assessments of adhesion at different material interfaces, on the other hand, have been developed. In particular, density-functional theory (DFT) has been widely applied to model interface decohesion in oxide/metal systems ([26] and references therein). The modeling has largely focused on computing the work of separation, γ, which is the reversible work required to separate an interface into two free surfaces neglecting plastic deformation. However, γ does not offer information about how the interfacial strength compares with the cohesion strength of the constituent materials. That comparison can be made indirectly using the original approach of U.R. Evans [19] where the elastically stored energy in the oxide scale resulting from stresses and strains in the oxide/metal system is compared to the energy which is needed to create two new surfaces in the form of a separation of the oxide from the metal substrate or of a through scale crack. In this regard, there is an interesting study reported by Qi and Hector [27,28] using first-principles calculations for Al/diamond interface where they emphasize the difference in energy needed to separate the two slabs of Al and diamond at the interface (work of separation) and the energy needed to fracture the joint set of the two slabs (work of decohesion). They showed that the work of decohesion is less than the cohesive energy of the bulk material, which was transferred from one slab to another and they also can predict the precise amount of adhered material and its relaxed geometry.

In the present work, we use DFT-based calculations to investigate adhesion at the $[100]\,(001)_{Fe}\|[110](001)_{Fe_3O_4}$ interface. Our calculations are focused on the γ at $T = 0$ K of three candidate interface geometries, including two terminations of the oxide and allowing for full atomic relaxations. In addition, this study analyzes the atomic and electronic structure of each interface. We then have an insight into the nature of the interface bonds through the application of several complementary analytical tools as electron localization function and charge density difference plots. The bond character and oxide surface termination effect on adhesion are carefully compared for each of the three candidate interface geometries and the structure of the Fe/Fe$_3$O$_4$ interface as suggested by our computed energetics is discussed.

2. Methods

Density-functional theory (DFT) [29,30] is used as implemented in the Vienna Ab-Initio Simulation Package (VASP) [31–33]. Ion–electron interactions are treated with projector augmented wave method (PAW) [34]. Plane wave expansions are considered with a cutoff energy of 500 eV. Exchange and correlation interactions are treated within the general gradient approximation (GGA) according to Perdew et al. [35]. Brillouin zone (BZ) integrations are based on a Monkhost–Pack grid (MP grid) [36]. Electronic occupancies are treated with the tetrahedron method with Blöchl corrections [37].

In studies of iron oxides, careful attention has to be paid to the treatment of the 3d electron correlation effect. The conventional DFT schemes that apply the GGA approximation underestimate the strong on-site Coulomb repulsion of the d electrons and consequently fail to capture the band gap depicted by the electronic structures of iron oxides, most of which are semiconductors. However, magnetite is nearly metallic, with a very narrow band gap (≈ 0.14 eV). It was only with the development of the GGA + U approximation [38] and hybrid functionals [35,39] that the pure GGA failures in calculations of iron oxides could be corrected [40,41]. However, two features concerning magnetite are not well reproduced by the GGA + U calculations using PAW: they lead to an overestimated band gap of 0.8 eV [40] and the authors showed that magnetite cubic structure has higher energy at $T = 0$ K than strained states meaning that the equilibrium cubic structure is elastically unstable [41]. Furthermore, both works conclude that the

standard DFT calculations with GGA and PAW might give reasonable predictions for structural and electronics parameters.

Total energy calculations in this work were performed at $T = 0$ K. Relaxation of atom positions was accomplished through a quasi-Newton algorithm for forces minimization till total forces attained values lower than 0.05 eV/Å per atom. Atomic structure plots were performed with VESTA [42].

3. Bulk and surface calculations

3.1. Bulk properties

Magnetite (Fe_3O_4) is a ferrimagnetic oxide with inverse spinel ($Fd3m$) structure at room temperature [43,44]. The internal degrees of freedom are fully relaxed to obtain the ground state unit cell as shown in Fig. 1. In this structure, oxygen can be found forming an FCC lattice, while iron is occupying the octahedral (Fe_A) and tetrahedral (Fe_B) interstices. These iron sublattices are antiferromagnetically coupled [45,46]. Along the (001) direction, atomic layers alternate their composition between Fe and FeO_2 (Fig. 1(b) and (c)). Iron has body center cubic ($Im3m$) structure at 293 K [47] with ferromagnetic behavior.

The MP grid was taken as $7 \times 7 \times 7$ for bulk magnetite and $15 \times 15 \times 15$ for BCC iron to get a convergence of 0.1 meV. Total energy is calculated as a function of the cell volume and fitted to a Birch–Murnaghan equation of state [48] to obtain the lattice parameter a, bulk modulus B_0 for both BCC iron and magnetite, the cohesive energy E_{coh} of the BCC iron and the formation energy ΔE_f of the magnetite.

For BCC iron, we find overbinding errors in lattice constant ($a_{Fe} =$ 2.842 Å; experiment at 298 K: 2.86 Å [49]) and cohesive energy ($E_{coh} = 4.85$ eV; experiment at 0 K: 4.28 eV [50]). This difference comes from systematic errors in the PAW-GGA approach to deal with the strongly correlated d electrons of iron ([40,41,51,52]). Instead, the bulk modulus is well estimated with respect to experiment ($B_0 =$ 173 GPa; experiment at room temperature: 164 GPa and 173 GPa [49], depending on the experimental method).

The structural and elastic parameters of the Birch–Murnaghan fit for magnetite exhibit excellent agreement with experiment ($a_{Fe_3O_4} =$ 8.395 Å and $x = 0.379$ Å; experiment at 130 K: 8.394 Å and 0.379 Å, respectively [53]; $B_0 = 169$ GPa; experiment at room temperature: 160–220 GPa [54], depending on the experimental method). The PAW-GGA treatment of the strongly correlated iron d electrons allowed an acceptable but not excellent agreement of formation energy value ($\Delta E_f = 1.29$ eV; experiment at room temperature: 1.65 eV [54]) and iron magnetic moments ($Fe_A = 3.4$ μ_B and $Fe_B = -3.4$ μ_B; experiment at 130 K: $Fe_A = 4.2$ μ_B and $Fe_B = -3.97$ μ_B [53]) with experimental ones.

3.2. Surface properties

Davenport et al. [5] obtained the orientation relationship between a BCC iron substrate and magnetite grown on it. They found that one of the most common orientation relationships is $[100] (001)_{Fe} \| [110] (001)_{Fe_3O_4}$. They observed that this relationship is related to the fact that in the [100] direction, the interatomic distances on BCC iron are almost equal to half the distances in the [110] direction of the oxide. Therefore, the Fe(001) and Fe_3O_4(001) planes have to be joined to form the metal/oxide interface.

Since our goal is to simulate the structure, energetics, and bonding at a bulklike interface, it is necessary for the interface slabs to be thick enough to exhibit bulklike interiors. This was accomplished by testing the convergence of the slab's surface energy with respect to slab thickness.

It is well known that the (001) surface of Fe exhibits a small degree of interlayer relaxation ($5 \pm 2\%$ of the bulk spacing [55]), while for Fe_3O_4 surface reconstruction has been observed experimentally [56], but the surface structure and stoichiometry are still under debate [57]. Then, we decided to do the convergence tests of the slab's surface energy with respect to slab thickness with unrelaxed supercells.

Our Fe(001) surface simulation cell has tetragonal geometry with one atom per layer, and the in-plane lattice vectors are consistent with the calculated bulk lattice parameter. A vacuum region was included in the supercell to prevent unwanted interactions between the slab and its periodic images. The convergence tests find that an 8 Å region is sufficient to converge the total energy of a twelve-layer slab with a $15 \times 15 \times 1$ k-point sampling in the BZ within 0.02 J/m². Following the method proposed by Boettger [58] to determine the minimum thickness necessary for a bulklike Fe slab, we have calculated the surface energy for slabs ranging from 4 up to 15 atomic layers. We found that the surface energy is well converged by a seven-layer thick slab with a value of 2.48 J/m², which is in good agreement with other DFT studies of BCC iron surfaces including also relaxation effects [59]. Afterwards, we performed the ionic relaxation of the slab with the parameters obtained from the convergence tests. All atoms within the slab were allowed to move. The final value for Fe(001) surface was 2.44 J/m².

The fracture of Fe_3O_4 along the plane (001) does not produce two symmetry equivalent surfaces (see Fig. 1). The same terminations for the oxide slab surfaces (i. e. same composition) implies that a non stoichiometric oxide slab must be used. Therefore, the Fe_3O_4(001) surfaces are modeled by symmetric slabs containing equal number of layers with Fe and FeO_2 composition and one additional layer with Fe or FeO_2 composition according to the surface composition that is considered for calculation. The vacuum between the repeated slabs amounts to 8 Å as in the BCC iron supercell. The dimensions of the supercell parallel
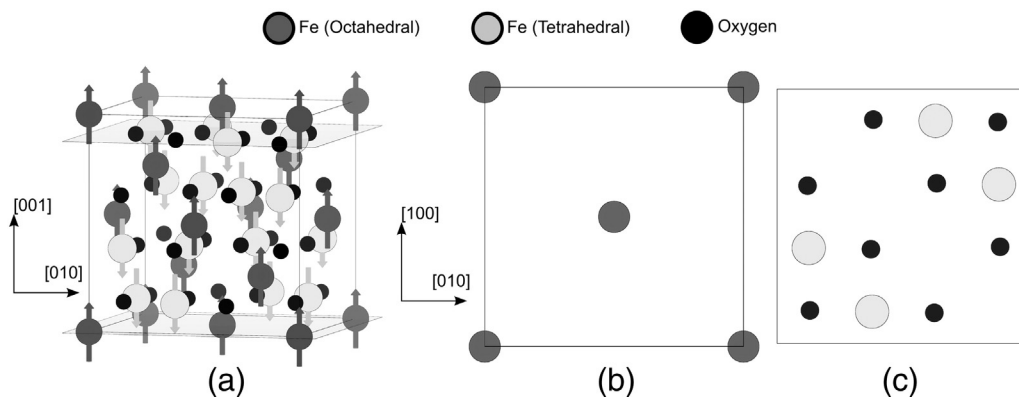

Fig. 1. (a) Magnetite unit cell with ($Fd3m$) structure. Arrows are placed on iron atoms to sketch antiferromagnetic spin ordering. Views of the (001) planes with (b) Fe composition and (c) FeO_2 composition.

to the slab surface have been set as equal to the GGA bulk lattice constant and the MP grid was taken as $7 \times 7 \times 1$. Although the use of equivalent surfaces at both endings of the oxide slab allows the generation of a nonpolar slab by design, a dipole correction was applied to check this hypothesis and the total energy correction was within the convergence criterion for the self-consistent cycle. Given the non-stoichiometry of the oxide slab, its surface energy needs to be computed in terms of chemical potentials of the elements present in the oxide and in equilibrium with an oxygen atmosphere. The surface energy is given by [60]:

$$\sigma(T, p) = \left(\frac{1}{A}\right) \left[G^{\text{surf}}(T, p, N_M, N_O) - N_M \, \mu_M(T, p) - N_O \, \mu_O(T, p) \right] \quad (1)$$

where A is the area of the oxide slab surfaces, G^{surf} is the Gibbs free energy of the oxide slab including the surfaces, and N_M and N_O are the number of metal and oxygen atoms within the non stoichiometric oxide slab. Since equilibrium must be held between surface and bulk, the chemical potentials are not independent variables and can be related to the free energy per atom in the bulk by means of the following relation:

$$x \, \mu_M(T, p) + y \, \mu_O(T, p) = g_{M_x O_y}^{\text{bulk}}(T, p) \quad (2)$$

where the small g denotes the Gibbs free energy per formula unit of the bulk oxide. Substituting Eq. (2) into Eq. (1), an expression is obtained for the surface energy depending only on the chemical potential of the oxygen μ_O

$$\sigma(T, p) = \left(\frac{1}{A}\right) \left[G^{\text{surf}}(T, p, N_M, N_O) - \frac{N_M}{x} \, g_{M_x O_y}^{\text{bulk}}(T, p) \right. \quad (3)$$
$$\left. - \left(N_O - \frac{y}{x} N_M \right) \mu_O(T, p) \right]$$

Using Eq. (3), the surface energy of any given metal–oxide surface can be calculated and its thermodynamic stabilities can be analyzed with respect to the given gas phase conditions. The value of μ_O has physical meaning only within certain boundaries. A suitable lower boundary, called the *O-poor limit*, is defined by the decomposition of the oxide into the pure metal and gas phase oxygen. In terms of thermodynamic quantities, this point is reached if the chemical potential of iron in the oxide bulk, μ_M, is lower than the chemical potential of iron in the pure metal, g_M^{bulk}. This upper bound for μ_M can be transformed into a lower bound of μ_O by using Eq. (2)

$$\mu_O(T, p) \geq \frac{1}{y} \left(g_{M_x O_y}^{\text{bulk}}(T, p) - x \, g_M^{\text{bulk}}(T, p) \right) \quad (4)$$

A reasonable upper bound of μ_O is given by such gas phase conditions that the condensation will start on the metal–oxide sample at low enough temperatures. This *O-rich limit* is defined here as

$$\mu_O \leq \frac{1}{2} E_{O_2}^{\text{tot}}$$

with $E_{O_2}^{\text{tot}}$ being the total energy of the oxygen gas phase. As shown by the detailed discussion of Rogal [60], in the calculation of the surface energy of a metal–oxide surface using Eq. (3), the leading terms are the total energies E^{total} of the different components, which are obtained directly from electronic structure calculations. A rough estimation of the remaining terms (the pV-term, the configurational entropy, and the vibrational contribution) showed that they are only of minor importance.

In order to test the convergence of the metal–oxide surface energy with increasing slab thickness, we calculated the surface energy in the *O-poor limit* obtained by inserting the right part of the inequality Eq. (4) into the expression for the surface energy Eq. (3)

$$\sigma_{O-\text{poor}}(T, p) = \left(\frac{1}{A}\right) \left[G^{\text{surf}}(T, p, N_M, N_O) - \frac{N_M}{x} \, g_{M_x O_y}^{\text{bulk}}(T, p) \right. \quad (5)$$
$$\left. - \left(\frac{1}{y} N_O - \frac{1}{x} N_M \right) \left(g_{M_x O_y}^{\text{bulk}}(T, p) - x g_M^{\text{bulk}}(T, p) \right) \right]$$

Fig. 2 illustrates the way in which the surface energy on the *O-poor* limit of unrelaxed $Fe_3O_4(001)$ surfaces converges with increasing slab thickness for both terminations considered. Values for the total energies per formula unit of the bulk oxide, $e_{Fe_3O_4}^{\text{bulk}}$, and bulk iron, e_{Fe}^{bulk}, were taken from separate converged bulk calculations. In the case of Fe termination, the variation of the surface energies as a function of slab thickness has an oscillatory character, which is also found in our calculations of Fe(001) surface energy and reported by other authors [59]. For slabs thicker than eleven layers, the convergence to the values given in Fig. 2 is within 0.03 J/m². The amount of 11 atomic layers for the oxide is the minimum required to represent one unit cell and to assure that both terminations have the same composition. This value of the converged slab thickness is equal to that found by the unrelaxed full-potential augmented plane wave calculations of Pentcheva and co-workers [61]. After this convergence test, we performed a full structural optimization of the atomic positions in the eleven-layer oxide slab for each surface termination. Both surface terminations suffer reconstruction, which is connected with an energy gain, the *O-poor* $Fe_3O_4(001)$ surface energies for relaxed slabs are 1.099 J/m² for the Fe termination and 1.012 J/m² for the FeO_2 termination.

Thermodynamic stabilities over the entire range of oxygen chemical potential for both terminations of the oxide surface become of interest due to their impact on the interfacial adhesion energies. The Eq. (3) is plotted in Fig. 3 for both Fe and FeO_2 terminations vs $\Delta\mu_O = \mu_O - (1/2) E_{O_2}^{\text{tot}}$ within the range given by the *O-poor* and *O-rich* limits. The value for $E_{O_2}^{\text{tot}}$ (9.86 eV) was calculated with VASP by placing an isolated O_2 molecule within a big box; spin polarization and ion position relaxation were considered. The FeO_2 termination turns out to be the most stable configuration even when, for oxygen-poor and relaxed conditions, it competes with the Fe termination. Accordingly, the results in Ref. [61] have identified the FeO_2 termination as the thermodynamically stable configuration over a broad range of oxygen pressures although in that work the relaxation of Fe-terminated surface was not considered.
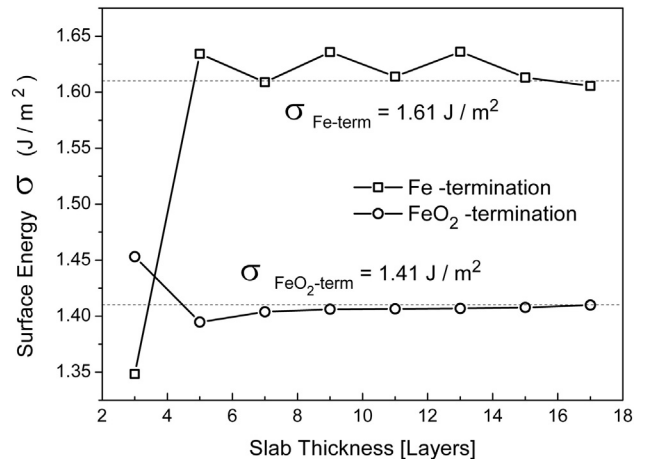

Fig. 2. *O-poor* surface energy per unit area calculated for Fe and FeO_2 terminated $Fe_3O_4(001)$ unrelaxed surfaces as a function of slab thickness.

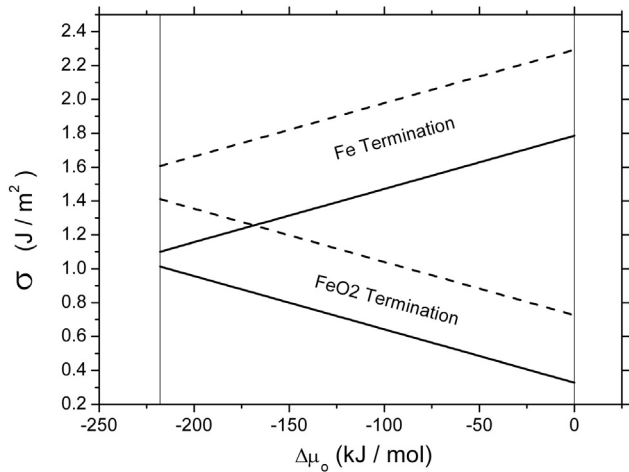**Fig. 3.** Surface energy vs chemical potential of the surrounding gas phase for Fe and FeO$_2$ terminated Fe$_3$O$_4$ (001) surfaces. The dashed lines apply to the unrelaxed surfaces while solid lines are for relaxed. Vertical lines indicate the limits for oxygen-poor (left) and oxygen-rich (right) atmospheres.

Since fracture energy can be stated as the energy necessary for cleavage, it can be alternatively understood as the energy necessary for creating two separated surfaces. By summing up unrelaxed

(relaxed) surface energies for both terminations, we obtain the value of 3.02 J/m^2 (2.11 J/m^2) for the fracture energy per unit area of magnetite in excellent agreement with the 3.01 J/m^2 (1.92 J/m^2) value reported by Liao and Carter [40].

In conclusion, we have shown that our calculated values of the bulk and surface properties for both Fe and Fe$_3$O$_4$ are in good agreement with other first-principles results, thereby validating the application of this methodology to the study of interfacial properties.

4. Interface calculations

4.1. Interface structure

Fig. 4 shows the model supercell used for interface calculations with sandwich model. Two equivalent interfaces are produced by the requirements of periodic boundary conditions. Oxide and metal slabs are located at each side of the interface with the orientations described above [5]. In the central region, 11 atomic layers form the oxide slab, while 7 atomic layers are disposed as the BCC iron slab.

The repeated distance along the [110] direction in the oxide, 2 × 2.968 Å, is close to twice the iron lattice parameter, 2 × 2.86 Å. However, the calculated lattice misfit of the interface is large (3.8%). The experiments presented in Ref. [5] showed that the passive oxide film on iron contains numerous extended defects, among which the authors mentioned: the finite crystallite size (~80 Å in-plane dimension and ~35 Å out of plane dimension) and the mosaic spread (2.5°), as
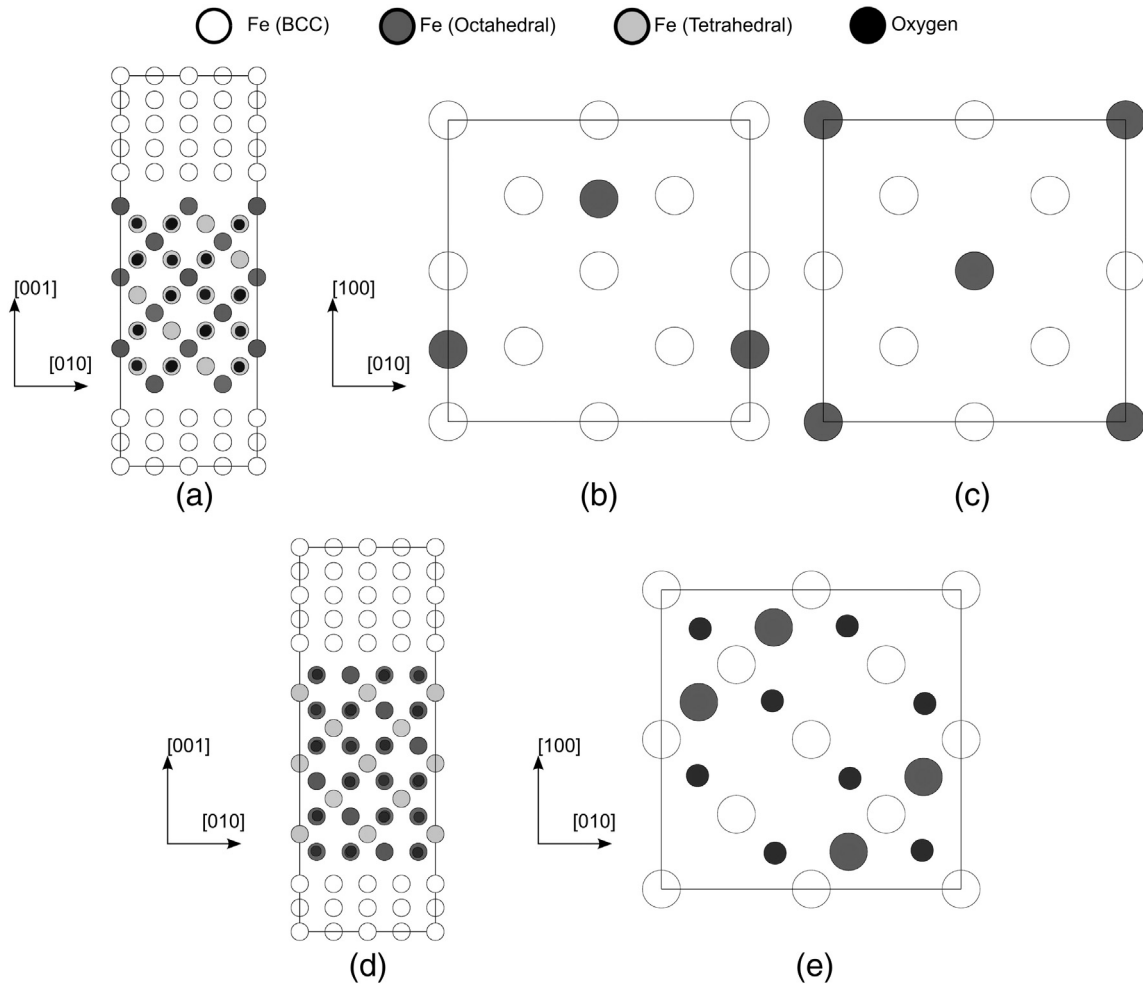

Fig. 4. Relative positions tested for the different oxide terminations. (a) Supercell sandwich model for the interface with Fe termination of the oxide in top stacking. (b) View of the atomic layers forming the interface with the hollow stacking. (c) Same as (b) but for the top stacking. (d) Supercell for the FeO$_2$ termination of the oxide. (e) Detailed view for the atomic stacking for this case. The coordinate systems refer to the oxide crystal.

well as the planar defects of antiphase boundaries (APBs) that form planes in the crystallites. The authors of this report were able to estimate the average distance between APBs which they found to be quite small (~20 Å, i.e., only a few unit cells). From these results, it can be suggested that there are large regions of coherency close to the interface, in which the oxide film is strained to match the dimensions of the metal substrate, separated by the extended defects. The specific problem of adhesion calculations is that if we were to accommodate this lattice misfit with one extended defect and satisfy the periodic boundary conditions, the minimum size of the supercell would be too large for fist principles computation. Therefore, the first-principles quantum-mechanical calculations are usually implemented using a small supercell and one unique lattice parameter for both materials that are in contact, i.e., straining the lattices into perfect coherency. Hence, misfit extended defects are artificially omitted. Our calculations use the coherent interface approximation, in which a compressive strain was introduced in the oxide along the [100, 010] directions to match the dimensions of the iron lattice parameter. As our interface simulations use the bulk GGA lattice constants, the 4.3% misfit in our system is somewhat larger than that which is found in experiment. Even though our estimates of interfacial bond character, atomic structure, and work of separation will be accurate for the regions between extended defects, the global work of separation may be overestimated by several tens percent as compared with the typical experimentally relevant semi coherent case [62].

As it was previously discussed, two terminations are possible for the oxide slab. For the iron terminated oxide, two stacking possibilities can be taken into account. In the hollow stacking (Fe term-hollow, Fig. 4(b)), iron atoms in the oxide surface are placed at a distance d above the octahedral sites of the metal surface. On the other hand, the top stacking (Fe term-top, Fig. 4(c)) is obtained by placing the iron atoms on the oxide surface over the iron atom on the metal surface. It can be observed that both stacking configurations differ in a translation of the oxide slab by a quarter of the lattice parameter along the [100] direction, as visualized in Fig. 4(b, c). Fig. 4(d, e) sketches the interface configuration for FeO_2 terminated oxide (FeO_2 term).

Magnetic coupling between contiguous slabs must be taken into account because BCC iron and magnetite are materials of strong magnetic nature. The oxide slab has antiferromagnetic ordering, that is, iron atoms in the two lattices Fe_A and Fe_B are antiferromagnetically coupled, but its two surfaces have equal composition; then the magnetic moment at both surfaces has the same global direction and the magnetic coupling with the iron slab in both interfaces may be parallel or antiparallel. These coupling possibilities are sketched in Fig. 5. The coupling was labeled as ferromagnetic (FM) when the alignment of BCC Fe and Fe_3O_4 magnetizations at each side of the interfaces is parallel while it was labeled as antiferromagnetic (AFM) in the other case. Hence, a test for energy differences among magnetic interface configurations was mandatory.

4.2. Work of separation

The key quantity to predict the mechanical properties of an interface is the work of separation γ, which is defined as the energy needed (per unit area) to reversibly separate an interface into two free surfaces [63], neglecting plastic and diffusional degrees of freedom. The energy needed in an actual cleavage experiment will always be greater than the work of separation due to plastic deformation. Formally, γ can be defined as the minimum of the interfacial energy E_{int} needed to separate the surfaces that conform the interface:

$$E_{\text{int}}(d) = \frac{1}{2A}\left[E(d) - \left(E_{\text{oxide}}^{\text{slab}} + E_{\text{metal}}^{\text{slab}}\right)\right] \tag{5}$$

where A is the surface area, $E(d)$ is the supercell total energy when the interfacial separation is d, and $E_{\text{oxide(metal)}}^{\text{slab}}$ are the isolated slab energies
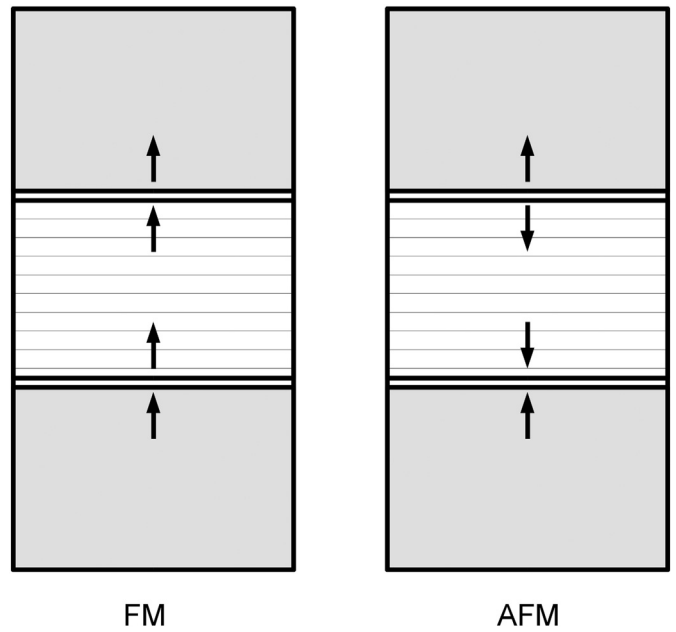

Fig. 5. Different magnetic couplings between the atomic layers forming the interface in the sandwich model. The gray (hatched) area represents metal (oxide). Arrows indicate the direction and sense of the magnetic moment of iron atoms in the layer of each slab contiguous to the interface.

for the oxide and the metal, respectively. The ½ factor is originated in the fact that two interfaces are present in the supercell. Calculation of the minimum interfacial energy and the equilibrium interfacial separation required relaxation of the interface structures. Our methodology for achieving this goal had two stages. The first step involved the calculation of the total energy of the sandwich model with an unrelaxed interface as the interfacial separation was reduced from an initially large value. The procedure followed until the energy passed through a minimum at the equilibrium separation and rose again for shorter distances. In these interface calculations, Brillouin zone integrations were performed in an MP grid of $7 \times 7 \times 1$ and, for each interfacial distance d, the ionic positions were not relaxed. The ab initio data were then fitted to the universal binding energy relation (UBER) [64], which is expressed in the following mathematical formula:

$$E_{\text{int}}(d) = -\gamma\left(1 + \frac{d - d_0}{l}\right)\exp\left(-\frac{d - d_0}{l}\right) \tag{6}$$

where d_0 is the equilibrium interfacial distance, γ is the work of separation, and l is a scale parameter. Results for γ and d_0 on the different systems are detailed on Table 1. Results for interfacial energy as a function of interface separation are shown in Fig. 6 for both studied terminations and both stacking configurations for the Fe termination of the oxide. Only FM coupling between contiguous slabs is shown. The differences in the interfacial energy due to FM or AFM coupling configuration were found to be 0.07 J/m² or less, while differences in energy between different atomic interface configurations are not less than 1.0 J/m². Besides, the work of separation follows the same intensity sequence for the three atomic configurations with FM coupling and AFM coupling. Therefore, we conclude that magnetic coupling has lower incidence in work of separation than atomic configuration.

The second step in our approach used the UBER interfacial geometries around the equilibrium distance as a starting point for obtaining the equilibrium geometry and minimum energy of the sandwich model with relaxed interface. The work of separation could then be estimated by finding the energy difference between the sandwich model with relaxed interface and the relaxed isolated slabs.

Table 1
Unrelaxed and relaxed work of separation (γ) and interface distances (d_0) for the three Fe(BCC)/Fe$_3$O$_4$ interface systems.

System	Fe$_3$O$_4$ termination	stacking	Unrelaxed (UBER)		Relaxed		
			γ (J/m^2)	d_0 (Å)	γ (J/m^2)	d_0 (Å)	Ref.
Fe(BCC)/Fe$_3$O$_4$	Fe	Hollow	1.93	1.29	1.44	1.16	This work
	Fe	Top	1.04	2.2	Unstable		This work
	FeO$_2$	–	1.41	1.9	1.40	2.11	This work
Low carbon steel/oxide					2		[24] (expt.)
Fe$_3$O$_4$/Fe$_3$O$_4$					>3		[40]

The values of γ and d_0 for all three interface structures, including both the unrelaxed (UBER) and relaxed geometries, are detailed on Table 1.

From UBER calculations, the configuration in which the oxide surface has composition Fe and the stacking of the oxide and metal is of the hollow type results to be that of greater cohesion, with a predicted value in good agreement with the experimentally measured value of 2 J/m^2 [24]. It is observed that the relative position of the atomic layers imprints a greater change in work of separation than the change in composition of the surface layers does.

As it can be seen in the table, the relaxed values are of the same order of magnitude as those predicted by the UBER, but two striking changes have occurred. First, the value of the work of separation is considerably reduced for Fe-terminated interface with hollow stacking while it remains equal for the FeO$_2$-terminated interface. In addition to this feature, there is also a noticeable increase of the difference between the values of the equilibrium interfacial separation of both interface types. Second, the relaxation of the geometry in the Fe-terminated interface with top stacking leads to completely unstable interface structures.

Considering our previous discussion about the energies for cleavage of Fe$_3$O$_4$ in different orientations and terminations obtained by Liao and Carter [40], a comparison with our values in Table 1 indicates that the oxide is more resistant than the Fe (BCC)/Fe$_3$O$_4$ interface. In this case, and according to Evans [65], a compression in the oxide layer and localized decohesion could cause oxide scale blistering, i.e., swelling that locally separates the oxide scale from the metal surface. The unwished effect would be the growth of the interfacial crack until the oxide spalls leaving an area of the metal unprotected.

4.3. Electronic structure and bonding

4.3.1. Electron localization

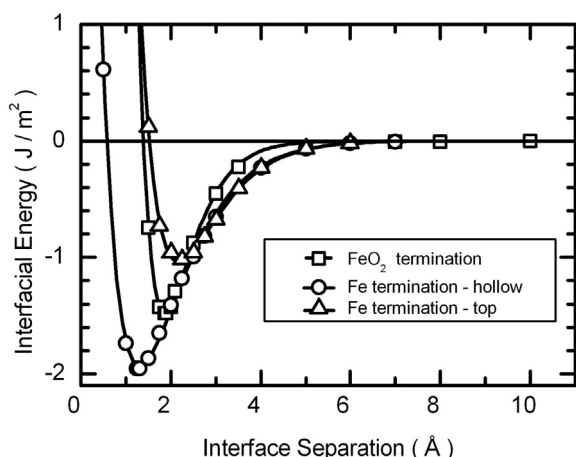In order to understand the adhesion results based on the characteristics of the chemical bonds involved, the electron localization function (ELF) [66,67] was calculated from VASP outputs for the different interface models. The ELF is a measure of the ratio between the electron pair probability density of the system and that of an electron gas. This measure is renormalized to be confined in the [0,1] interval, in such a way that in the region where ELF is close to 0.5, an electron gas-like behavior can be expected. In the other hand, the region where ELF is close to 1 is said to resemble a covalent bond (strong localization), and when ELF is close to 0, there is a low probability of finding electron pairs (zero localization). We have adopted for figures a color scale in which white zones stand for small values and black zones for high values, with an intermediate gray zone. The isolines divide the ELF range in ten sub-ranges of equal size.

Fig. 7 shows an ELF plot for the interface where the oxide is terminated in Fe and the metal is placed in the hollow type stacking. Three parallel and consecutive (110) slices have been chosen. The first one (110)$_A$ includes an oxygen row from the oxide subsurface layer in interaction with the terminal layer of the metal, with no more atoms in between. The second slice (110)$_B$ is chosen to include a row of tetrahedral irons from the terminal layer in the oxide just below the octahedral sites in the metal. The third slice (110)$_C$ is similar to (110)$_B$, but the contact is between octahedral iron atoms in the oxide and the octahedral sites in the bcc metal. It is observed that the electron gas (gray colored region) from the iron slab is extended into the oxide subsurface, not only embracing the terminal iron layer in the oxide but also creating a bond with the iron atoms in the layer immediately below. This observation suggests that shared metallic bonds between the metal iron and tetrahedral or octahedral irons from the oxide are responsible for the main properties of the interface.

As seen in Fig. 8, the relaxation of the atomic forces also causes the rippling of the atoms at both sides of the interface formed with the FeO$_2$ terminated oxide slab. The ripple on the interface at the oxide side is mainly due to the movement of oxygen atoms towards the surface of Fe (BCC). A lateral wavelike distortion of the oxygen rows is also evidenced towards the octahedral Fe atoms rows. A similar distortion had been detected on the surface of the isolated oxide [61]. The three parallel (110) slices in Fig. 8 were chosen in order to show, first, the interaction between a row of terminal iron in the metal surface with a row of oxygen atoms in the oxide terminal layer and intercalated tetrahedral irons in the oxide subsurface (slice (110)$_A$); second, the interaction between a row of octahedral Fe atoms of the oxide surface with an atomic row of the subsurface (slice (110)$_B$); lastly, the interaction between an oxygen row of the oxide surface and an iron row within the metal (slice (110)$_C$). In this case, the electron gas is not extended into the inner layers of the oxide, no bonding is observed with the subsurface layer, and bonding appears only between the metal slab and the iron in the terminal oxide layer. The penetration of the metallic cloud into the oxide structure might then be responsible for the higher work of separation in hollow stacking configuration.

4.3.2. Charge density difference plots

To support these observations, charge density difference (CDD) was calculated subtracting the superposition of isolated atoms from the ground state charge density obtained from DFT calculations. This technique is widely used in literature to investigate bonding characteristics on many complex systems in the basis of charge redistribution and
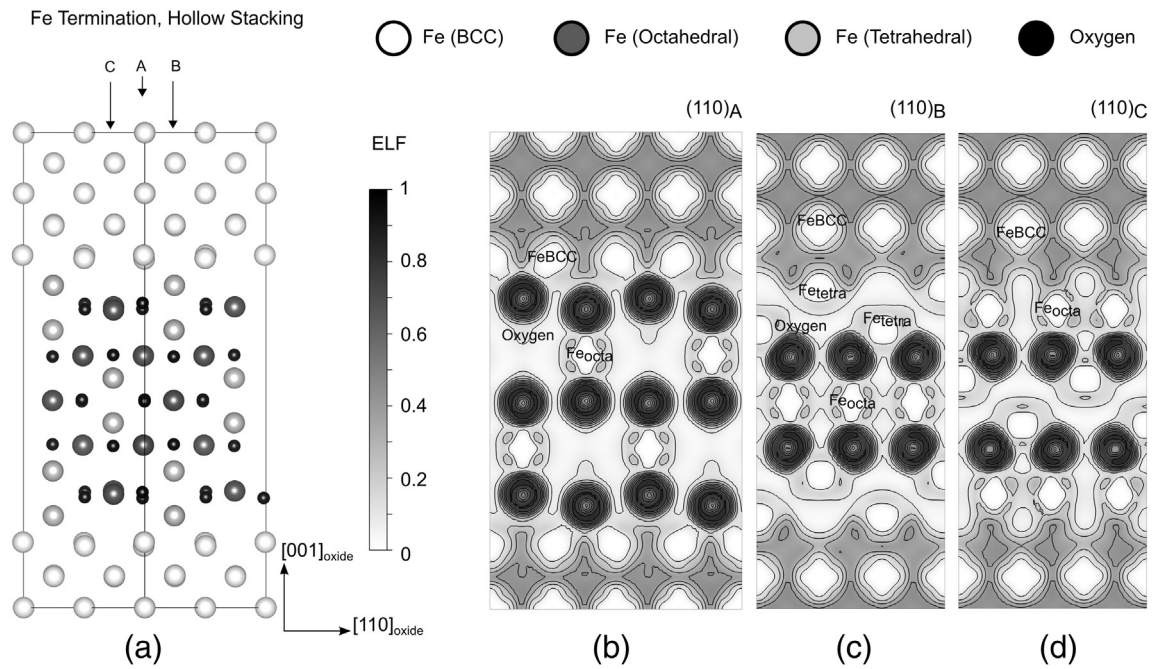
Fig. 6. UBER curves, from total energy calculations as a function of interfacial separation.

Fe Termination, Hollow Stacking

○ Fe (BCC)　● Fe (Octahedral)　● Fe (Tetrahedral)　● Oxygen

Fig. 7. Electron localization function (ELF) maps for interface with the Fe-terminated magnetite, hollow stacking. (a) A view of the supercell oriented in such a way that the (110) planes are perpendicular to the view. A, B, and C (110) parallel slices are indicated; ELF maps projected on (b) A slice, (c) B slice, and (d) C slice. Localization increases from white to black zones. The position of ticks on the gray scale indicates the values for isolines. The coordinate system refers to oxide crystal.

makes it possible to identify particular atoms involved in a certain chemical bond. For instance, Siegel et al. [68,69] implemented this method to explain interfaces properties from DFT calculations and used topological arguments to find failure modes in metal–metal and metal–oxide interfaces. CDD plots are obtained for Fe and FeO_2 terminations for the same planes and stacking modes chosen for the ELF slices, as shown in Figs. 9 and 10.

Bonding across the interface in iron terminated hollow stacking (Fig. 9) is reflected in charge accumulation between iron atoms on both sides (light gray lobes in Fig. 9$(110)_B$ and $(110)_C$). At the oxide side, both tetrahedral and octahedral iron atoms are involved in the bonding. In the center layer of the oxide slab, the charge accumulation at oxygen atoms sites shows the polarization of the covalent bond with the tetrahedral and octahedral iron atoms. This charge distribution changes drastically in the oxide subsurface layer (see Figure $(110)_A$) due to the metallic bonding between iron atoms on metal and oxide slabs. Both effects thus contribute to form a mixed covalent/metallic interfacial bond.
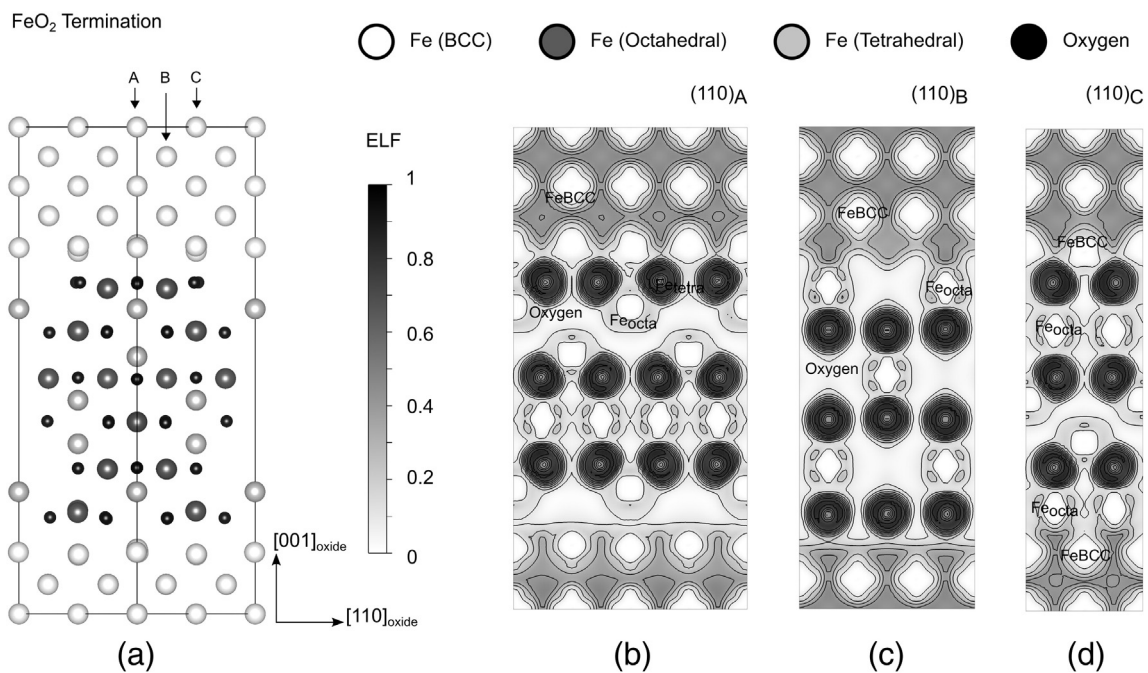
FeO_2 Termination

○ Fe (BCC)　● Fe (Octahedral)　● Fe (Tetrahedral)　● Oxygen

Fig. 8. Electron localization function (ELF) maps for interface with the FeO_2 terminated magnetite. (a) A view of the supercell oriented in such a way that the (110) planes are perpendicular to the view. A, B, and C (110) parallel slices are indicated; ELF maps projected on (b) A slice, (c) B slice, and (d) C slice. Localization increases from white to black zones. Position of ticks on the gray scale indicates the values for isolines. The coordinate system refers to oxide crystal.
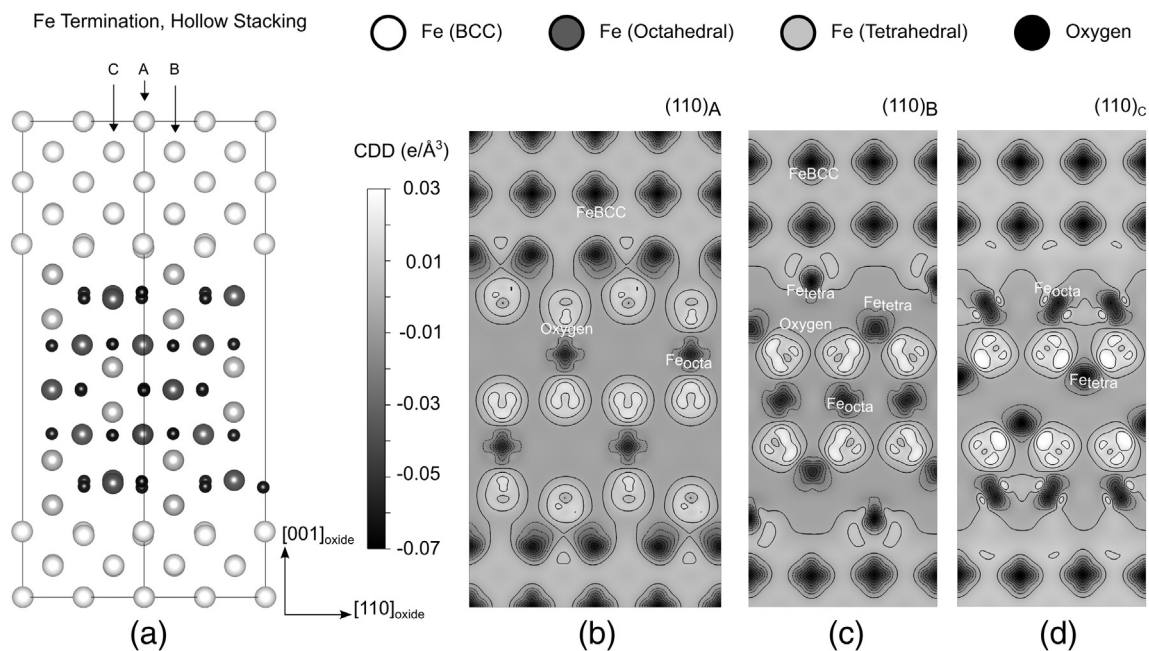
Fe Termination, Hollow Stacking   ○ Fe (BCC)   ◔ Fe (Octahedral)   ○ Fe (Tetrahedral)   ● Oxygen

Fig. 9. Charge density difference (electrons/Å³) plots for Fe-terminated magnetite with hollow stacking. (a) A view of the supercell oriented in such a way that the (110) planes are perpendicular to the view. A, B, and C (110) parallel slices are indicated; CDD plots projected on (b) A slice, (c) B slice, and (d) C slice. The coordinate system refers to oxide crystal.

The CDD plots for the interface where the oxide is terminated in FeO_2 (Fig. 10) exhibit some features in common with the CDD plots analyzed in the previous paragraph. However, only the octahedral iron atoms are involved in the bonding with the Fe(BCC) atoms (see Fig. 10 $(110)_B$ and $(110)_C$). As a consequence, only the polarization of the covalent bond between oxygen and octahedral iron atoms is modified in the oxide interface layer. A weaker interaction can thus be expected in this case.

4.3.3. Density of states

Density of state (DOS) plots can give us further insight into the role of atoms according to theirs type, magnetic moment, and site with respect to bonding. In order to perform a quantitative and qualitative analysis, site, and layer, projected DOS were obtained from our spin polarized DFT calculations. Fig. 11 shows the projected DOS for the different atomic species present in the atomic layers at different distances from the interface towards the material bulk. The population of d states is asymmetric with respect to spin orientation in the center layer of both slabs, but the asymmetry is weak in the metal slab while it is strong in the oxide one. The asymmetry is associated with the orientation and magnitude of the magnetic moment. FM (AFM) coupling between slabs was imposed by setting the same (opposed) sense of the magnetic moment for iron atoms on the layers contiguous to the interface on both slabs. Then the same spin up or down was initially assigned to all iron
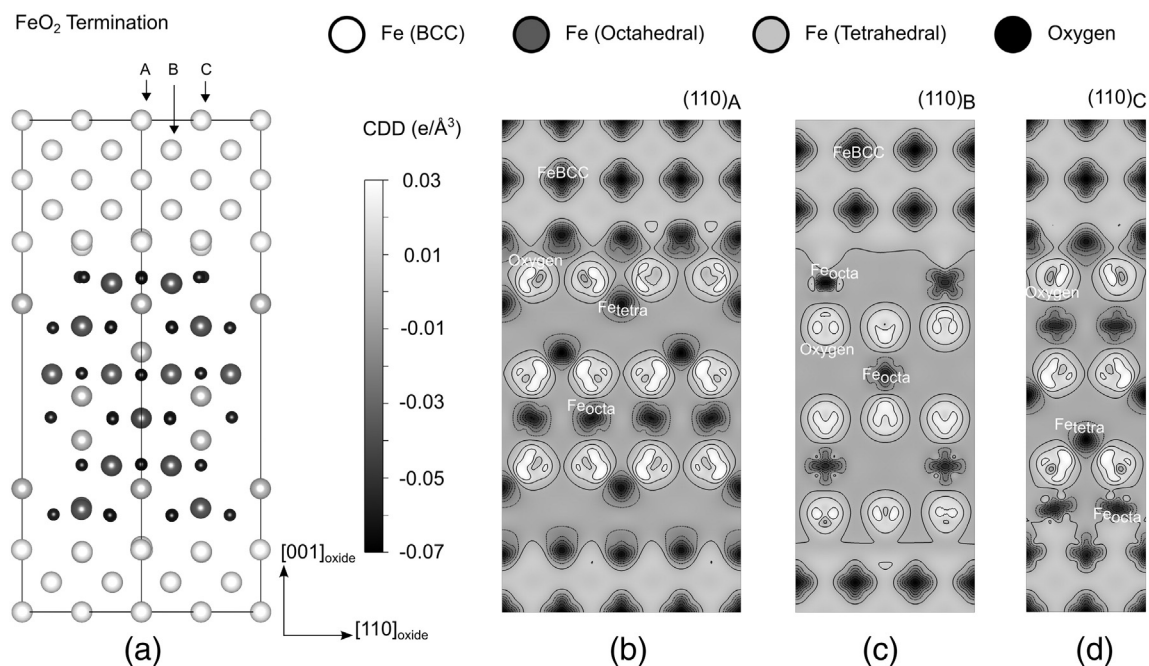
FeO_2 Termination   ○ Fe (BCC)   ◔ Fe (Octahedral)   ○ Fe (Tetrahedral)   ● Oxygen

Fig. 10. Charge density difference (electrons/Å³) plots for FeO_2 terminated magnetite. (a) A view of the supercell oriented in such a way that the (110) planes are perpendicular to the view. A, B, and C (110) parallel slices are indicated; CDD plots projected on (b) A slice, (c) B slice, and (d) C slice. The coordinate system refers to oxide crystal.
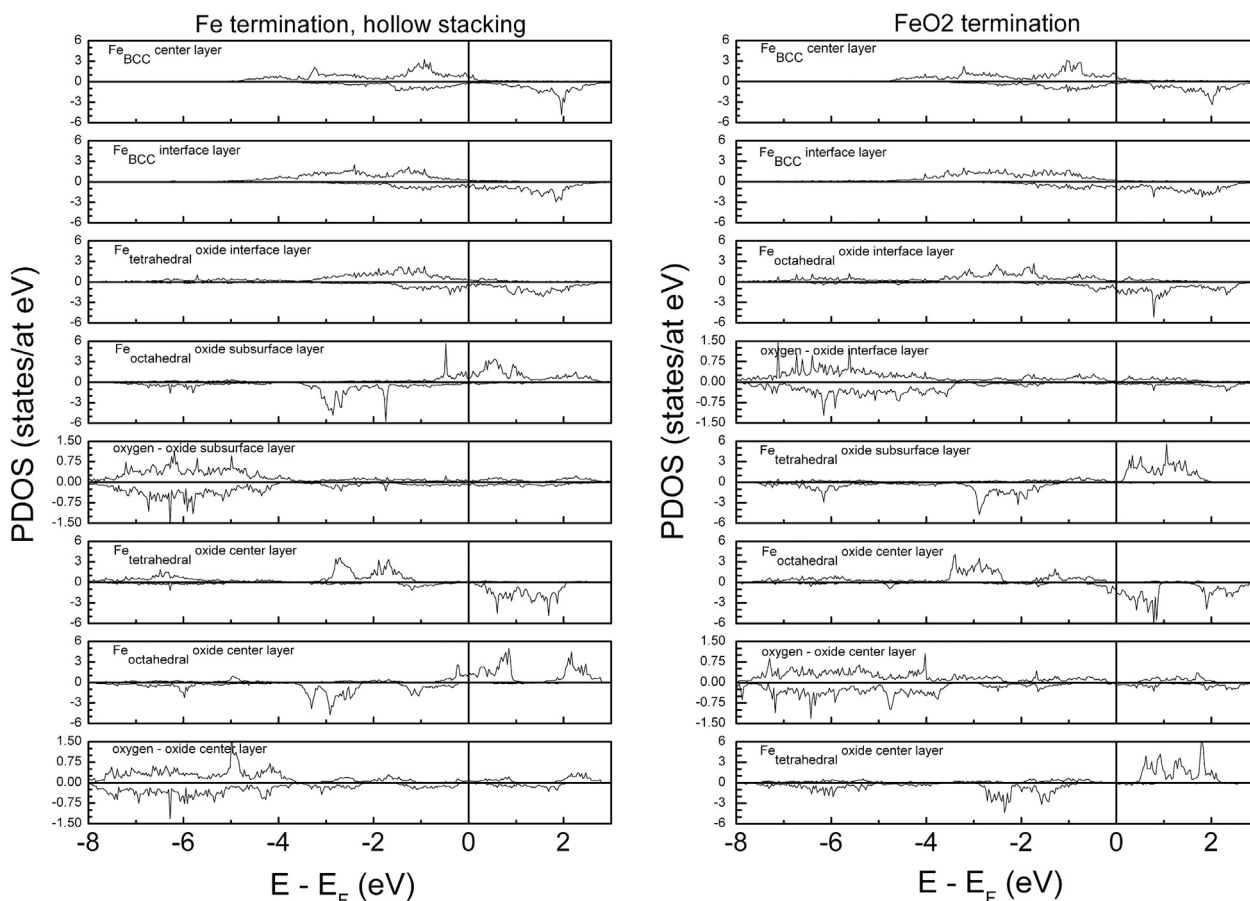
Fig. 11. Projected density of states on atomic layers (states/at eV) vs energy (eV) plots. Each plot corresponds to the partial DOS projected on all the equivalent atoms in the corresponding atomic layer. For Fe atoms d-band is considered, while p-band is shown for oxygen. Solid vertical lines denote the position of the Fermi level.

atoms within the oxide equivalent to the one on the interface (tetrahedral or octahedral). This imposed magnetic coupling between slabs is still evident after self consistency cycle through the majority spin agreement between iron sites at the center of the metal slab and iron sites at the center of the oxide slab. On the contrary, iron atoms at the oxide interface layer appears remarkably affected. After this analysis, both examples shown in Fig. 11 correspond to a ferromagnetic coupling between the slabs.

When the composition of the oxide terminal layer is pure Fe (tetrahedral iron), and the stacking is in the hollow position, iron atoms on either side of the interface reduces their magnetic moments due to a change in spin populations. Electron states with spin up are lost in the BCC iron while the tetrahedral iron gains electron states with spin down. In addition, tetrahedral iron undergoes a strong redistribution of the density of states with spin up. This redistribution has consequences for the covalent bonds between iron and oxygen atoms belonging to both the interface and the subsurface layer. The octahedral iron and oxygen atoms at the subsurface layer clearly show two new states in the energy range between the Fermi level and −2 eV, one for each spin channel, showing the changes in the hybridization between Fe 3d and O 2p states. In turn, for energies below −4 eV, the spin up Fe 3d states in the tetrahedral iron atom decrease significantly their intensities while the O 2p states increase their intensities in the same spin channel. The band gap in the Fe 3d states of tetrahedral iron atoms is modified substantially in the interface and some electronic states appear in the conduction band pointing out the ionic–metallic character of the bonding between the metal and oxide slabs, while the covalent binding component is weak.

The PDOS plots of Fig. 11 for the FeO$_2$-terminated interface support the conclusions about the interfacial bonding between the metal and

the oxide obtained from the analysis of the CDD and ELF results. The role played by tetrahedral iron atom within the iron terminated oxide situation is now fulfilled by the octahedral atom in the interfacial oxide layer. It gains electron states with spin down and undergoes a redistribution of the density of states with spin up in order to reduce its magnetic moment. On the other hand, the density of states of tetrahedral iron in the oxide subsurface layer shows only small changes. The new states with spin down in the PDOS of the octahedral atom at the interfacial oxide layer appears to come from changes in the covalent bond with the oxygen of the same layer, as seen from the change in its spin down population along the range of energies below the Fermi level and up to −4 eV. In addition, the number of states at the Fermi level does not undergo great modifications. Therefore, the interfacial bonding appears to be a mixed covalent/metallic bond.

5. Summary and conclusions

We have gained a basic understanding of the adhesion at the Fe(BCC)/Fe$_3$O$_4$ interface from first-principles density-functional theory. The interrelations between interfacial atomic structure and work of separation have been discussed. The following specific findings have been described:

(i) Our primary finding is that, regardless of the oxide slab termination, the dominant bonding mechanism is the metallic-ionic interaction between the iron atoms of the metal and oxide slabs. A small degree of covalency could be involved; this contribution comes from modifications of the covalent bond between the oxygen and iron atoms in the interface and/or subsurface layer of the oxide slab.

(ii) The work of separation seems to be independent of the interfacial stoichiometry. The explanation is found in the interfacial bonding

described above. The two stable interfaces try to maximize the number of Fe(BCC)–Fe(magnetite) bonds, so the Fe-terminated interface needs to involve the Fe octahedral atoms at the subsurface layer to match the number of bonds reached for the FeO$_2$-terminated interface.

(iii) The value of the work of separation is in good agreement with scarce experimental results available for interfacial fracture energy measured at room temperature.

Recently, research on bi-material interfaces has aspired to construct a computational framework for predicting the interface toughness by starting from basic aspects of atomic bonding [70–72]. This modeling considered a cohesive zone embedded within an elastic/plastic finite element scheme for calculating the fracture resistance. The tractions on the boundary of the cohesive zone are matched with those derived from energy–displacement curve for the interface calculated using DFT. From this assumption, the work of separation γ and the maximum interfacial strength σ emerge as the primary parameters to bridge from the microscopic to macroscopic scale in interface fracture. Our current results only provide the value of γ, the full energy–displacement curve for both relaxed interfaces in order to obtain the respective σ values is under work. These results could also help to overcome our limitations regarding the temperature of the system. Calculations at temperatures above 0 K require Born $-$ Oppenheimer molecular dynamics simulations. Such ab initio calculations involve heavily computational task and thus is quite time-consuming. Molecular dynamics simulation using empirical potential for interatomic interaction reduces calculation time and thus enables the study of a large atomic system. In general, the empirical potential function can be obtained by fitting the measured data of material's bulk properties from experiments. However, the experimental information for heterogeneous interface is quite scarce. For this reason, at least two methodologies for generating the heterogeneous interface pair potential were proposed by fitting the energy–displacement curve obtained from ab initio calculations [73,74].

Acknowledgments

References

[1] J.W. Schultze, M.M. Lohrengel, Electrochim. Acta 45 (2000) 2499.
[2] C. Olsson, Electrochim. Acta 48 (2003) 1093.
[3] N. Sato, Corros. Sci. 31 (1990) 1.
[4] L.J. Oblonsky, J. Electrochem. Soc. 144 (1997) 2398.
[5] A.J. Davenport, L.J. Oblonsky, M.P. Ryan, M.F. Toney, J. Electrochem. Soc. 147 (2000) 2162.
[6] M. Toney, A.J. Davenport, L. Oblonsky, M. Ryan, C. Vitus, Phys. Rev. Lett. 79 (1997) 4282.
[7] W. Yi, W. MoberlyChan, V. Narayanamurti, Y.F. Hu, Q. Li, I. Kaya, M. Burns, D.M. Chen, J. Appl. Phys. 95 (2004).
[8] B. Beverskog, M. Bojinov, A. Englund, P. Kinnunen, T. Laitinen, K. Mäkelä, T. Saario, P. Sirkiä, Corros. Sci. 44 (2002) 1901.
[9] R.Y. Chen, W.Y.D. Yuen, Oxid. Met. 59 (2003) 433.
[10] H. Sakai, T. Tsuji, K. Naito, J. Nucl. Sci. Technol. 22 (1985) 158.
[11] G.S. Frankel, N. Sridhar, Mater. Today 11 (2008) 38.
[12] R. Tapping, J. Nucl. Mater. 383 (2008) 1.
[13] M. Kiran Kumar, K. Gaonkar, S. Ghosh, V. Kain, M. Bojinov, T. Saario, J. Nucl. Mater. 401 (2010) 46.
[14] X. Yu, Z. Jiang, X. Wang, D. Wei, Q. Yang, Adv. Mater. Res. 415-417 (2012) 853.
[15] K. Voges, A. Mueth, S.M. Street, B. Lehane, S. Critchley, Iron Steel, Technol. Conf. Expo., AISTech, 2007 2007 (Indianapolis).
[16] D. Genève, D. Rouxel, P. Pigeat, M. Confente, Corros. Sci. 52 (2010) 1155.
[17] P. Gillström, M. Jarl, Scand. J. Metall. 33 (2004) 269.
[18] M. Krzyzanowski, W. Yang, C.M. Sellars, J.H. Beynon, Mater. Sci. Technol. 19 (2003) 109.
[19] M. Schütze, P.F. Tortorelli, I.G. Wright, Oxid. Met. 73 (2010) 389.
[20] M. Schütze, Mater. High Temp. 22 (2005) 147.
[21] K. Miyoshi, B. Pohlchuck, N.C. Whittle, L.G. Hector, J. Adams, Properties Data for Adhesion and Surface Chemistry of Aluminum(NASA Techn) 1998.
[22] J. Mougin, M. Dupeux, A. Galerie, L. Antoni, Mater. Sci. Technol. 18 (2002) 1217.
[23] F. Toscan, L. Antoni, Y. Wouters, M. Dupeux, A. Galerie, Mater. Sci. Forum 461-464 (2004) 705.
[24] T. Nilsonthi, S. Chandra-ambhorn, Y. Wouters, A. Galerie, Oxid. Met. 79 (2013) 325.
[25] A. Galerie, F. Toscan, E. N'Dah, K. Przybylski, Y. Wouters, M. Dupeux, Mater. Sci. Forum 461-464 (2004) 631.
[26] J.I. Beltrán, M.C. Muñoz, Phys. Rev. B - Condens. Matter Mater. Phys. 78 (2008) 1.
[27] Y. Qi, L.G. Hector, Phys. Rev. B 68 (2003) 201403.
[28] Y. Qi, L.G. Hector, Phys. Rev. B 69 (2004) 235401.
[29] P. Hohenberg, W. Kohn, Phys. Rev. 136 (1964) B864.
[30] W. Kohn, L.J. Sham, Phys. Rev. 140 (1965) A1133.
[31] G. Kresse, J. Hafner, Phys. Rev. B 47 (1993) 558.
[32] G. Kresse, J. Furthmüller, Phys. Rev. B 54 (1996) 11169.
[33] G. Kresse, J. Furthmüller, Comput. Mater. Sci. 6 (1996) 15.
[34] D. Vanderbilt, Phys. Rev. B 41 (1990) 7892.
[35] J.P. Perdew, K. Burke, M. Ernzerhof, D. of Physics, N.O.L. 70118 J. Quantum Theory Group Tulane University, Phys. Rev. Lett. 77 (1996) 3865.
[36] H.J. Monkhorst, J.D. Pack, Phys. Rev. B 13 (1976) 5188.
[37] P.E. Blöchl, O. Jepsen, O.K. Andersen, Phys. Rev. B 49 (1994) 16223.
[38] S.L. Dudarev, G.A. Botton, S.Y. Savrasov, C.J. Humphreys, A.P. Sutton, Phys. Rev. B 57 (1998) 1505.
[39] A.D. Becke, J. Chem. Phys. 98 (1993).
[40] P. Liao, E. a. Carter, J. Mater. Chem. 20 (2010) 6703.
[41] H. Guo, A.S. Barnard, Phys. Rev. B—Condens. Matter Mater. Phys. 83 (2011) 1.
[42] K. Momma, F. Izumi, J. Appl. Crystallogr. 44 (2011) 1272.
[43] M.E. Fleet, Acta crystallogr. Sect. B Struct. Crystallogr. Cryst. Chem. 37 (1981) 917.
[44] J.P. Wright, P.G. Radaelli, Phys. Rev. B 66 (2002) 1.
[45] A.D. Rowan, C.H. Patterson, L. V Gasparov, Phys. Rev. B 79 (2009) 205103.
[46] Z. Zhang, S. Satpathy, Phys. Rev. B 44 (1991) 13319.
[47] W.B. Pearson, W.B.B.T.-A.H. of L.S. and S. of M. and A. Pearson, Int. Ser. Monogr. Met. Phys. Phys. Metall., Pergamon, 1958 123.
[48] F. Birch, J. Appl. Phys. 9 (1938).
[49] D.R. Wilburn, W. Abassett, Am. Mineral. 63 (1978) 591.
[50] C. Kittel, Introduction to Solid State Physics, eighth ed. John Wiley & Sons, Inc., 2005
[51] N.J. Mosey, P. Liao, E.A. Carter, J. Chem. Phys. 129 (2008) 014103.
[52] C. Rödl, F. Fuchs, J. Furthmüller, F. Bechstedt, Phys. Rev. B 79 (2009) 235114.
[53] J.P. Wright, J.P. Attfield, P.G. Radaelli, Phys. Rev. B 66 (2002) 214422.
[54] C. Haavik, S. Stølen, H. Fjellvåg, M. Hanfland, D. Häusermann, Am. Mineral. 85 (2000) 514.
[55] Z.Q. Wang, Y.S. Li, C.K.C. Lok, J. Quinn, F. Jona, P.M. Marcus, Solid State Commun. 62 (1987) 181.
[56] B. Stanka, W. Hebenstreit, U. Diebold, S. A. Chambers, Surf. Sci. 448 (2000) 49.
[57] M. Fonin, R. Pentcheva, Y.S. Dedkov, M. Sperlich, D.V. Vyalikh, M. Scheffler, U. Rüdiger, G. Güntherodt, Phys. Rev. B: Condens. Matter Mater. Phys. 72 (2005) 1.
[58] J. Boettger, Phys. Rev. B 49 (1994) 798.
[59] P. Błoński, A. Kiejna, Surf. Sci. 601 (2007) 123.
[60] J. Rogal, Stability, Composition and Function of Palladium Surfaces in Oxidizing Environments, A First-Principles Statistical Mechanics Approach; Ph.D. Thesis, Physics Department, Freie Universität Berlin, 2006.
[61] R. Pentcheva, F. Wendler, H.L. Meyerheim, W. Moritz, N. Jedrecy, M. Scheffler, Phys. Rev. Lett. 94 (2005) 126101-1.
[62] J. Schnitker, D.J. Srolovitz, Model. Simul. Mater. Sci. Eng. 6 (1998) 153.
[63] M.W. Finnis, J. Phys, Condens. Matter 8 (1999) 5811.
[64] J.H. Rose, J. Ferrante, J.R. Smith, Phys. Rev. Lett. 47 (1981) 675.
[65] H.E. Evans, Mater. Sci. Technol. 4 (1988) 415.
[66] B. Silvi, A. Savin, Nature 371 (1994) 383.
[67] A.D. Becke, K.E. Edgecombe, J. Chem. Phys. 92 (1990) 5397.
[68] D. Siegel, L. Hector, J. Adams, Phys. Rev. B 65 (2002) 085415.
[69] D.J. Siegel, L.G. Hector, J.B. Adams, Acta Mater. 50 (2002) 619.
[70] J.W. Hutchinson, Wei Yueguang, Int. J. Fract. 95 (1999) 1.
[71] Y. Jiang, Y. Wei, J.R. Smith, J.W. Hutchinson, A.G. Evans, Int. J. Mater. Res. 101 (2010) 8 (formerly Zeitschrift Fuer Met.).
[72] F. Cordisco, P.D. Zavattieri, L.G. Hector, A.F. Bower, Eng. Fract. Mech. 131 (2014) 38.
[73] Y. Long, N.X. Chen, J. Phys. Condens. Matter 19 (2007) 196216.
[74] A.C.T. van Duin, A. Strachan, S. Stewman, Q. Zhang, X. Xu, W.A. Goddard III, J. Phys. Chem. A 107 (2003) 3803.